AGU PUBLICATIONS

JGR

Journal of Geophysical Research: Oceans

RESEARCH ARTICLE

10.1002/2015JC011503

Key Points:
- Altimeter data errors
- Spectral analysis
- Dynamics and modeling

Correspondence to:
D. Stammer,
detlef.stammer@uni-hamburg.de

Citation:
Biri, S., N. Serra, M. G. Scharffenberg, and D. Stammer (2016), Atlantic sea surface height and velocity spectra inferred from satellite altimetry and a hierarchy of numerical simulations, *J. Geophys. Res. Oceans*, *121*, 4157–4177, doi:10.1002/2015JC011503.

Received 25 NOV 2015
Accepted 14 MAY 2016
Accepted article online 19 MAY 2016
Published online 18 JUN 2016

Atlantic sea surface height and velocity spectra inferred from satellite altimetry and a hierarchy of numerical simulations

Stavroula Biri[1], Nuno Serra[1], Martin G. Scharffenberg[1], and Detlef Stammer[1]

[1]Institut für Meereskunde, Centrum für Erdsystemforschung und Nachhaltigkeit, Universität Hamburg, Germany

Abstract Frequency and wavenumber spectra of sea surface height (SSH) and surface geostrophic velocity are presented, as they result for the Atlantic Ocean from a 23 year long altimeter data set and from a hierarchy of ocean model simulations with spatial resolutions of 16, 8, and 4 km. SSH frequency spectra follow a spectral decay of roughly f^{-1} on long periods; toward higher frequencies a spectral decay close to f^{-2} is found. For geostrophic velocity spectra, a somewhat similar picture emerges, albeit with flatter spectral relations. In terms of geostrophic velocity wavenumber spectra, we find a general relation close to k^{-3} in the high-resolution model results. Outside low-energy regions all model spectra come close to observed spectra at low frequencies and wavenumbers in terms of shape and amplitude. However, the highest model resolution appears essential for reproducing the observed spectra at high frequencies and wavenumbers. This holds especially for velocity spectra in mid and high latitudes, suggesting that eddy resolving ocean models need to be run at a resolution of 1/24° or better if one were to fully resolve the observed mesoscale eddy field. Causes for remaining discrepancies between observed and simulated results can be manifold. At least partially, they can be rationalized by taking into account an aliasing effect of unresolved temporal variability in the altimetric observations occurring on periods smaller than the 20 days Nyquist period of the altimetric data, thereby leading to an overestimate of variability in the altimetric estimates, roughly on periods below 100 days.

1. Introduction

The ocean is a turbulent fluid. To fully understand its dynamics and to adequately quantify the implications of its broadband variability for many applications (including the interaction of the physical flow field with the ecosystem, biogeochemistry, or simply air-sea interaction), one needs to describe the statistics of its variability, e.g., in terms of dominant space and time scales. An efficient approach in this context is a spectral description of the ocean variability [*Wortham and Wunsch,* 2014]. Ideally, such a description should be based on long-time series obtained with high temporal sampling rates with spatial resolution adequately sampling energetic features such as eddies; however, observations sampled simultaneously with high spatial and temporal resolution are not yet available, even in the presence of many satellite missions. Investigations of ocean variability therefore continue to heavily rely on a combined analysis of observations of ocean variables and respective model simulations.

In a pioneering attempt to study the ocean eddy field from observations, *Wunsch* [1981] provided first frequency spectra based on moored current meter data. Several other studies followed, among them the analysis of *Stammer* [1997], who calculated sea surface height (SSH), sea surface slope, and geostrophic velocity spectra in the frequency and wavenumber domains utilizing the measurements of the first 3 years of the TOPEX/Poseidon altimetric mission. Results contributed to a better description of the frequency characteristics of the flow field on a global and regional scale. More recently, *Ferrari and Wunsch* [2009] synthesized spectral density estimates of horizontal kinetic energy available from in situ observations on periods below the annual cycle. Their results display a broad band of nearly white low-frequency flow variability at periods longer than 40 days. Toward higher frequencies, variability levels fall off in the so-called geostrophic eddy range with an approximate power law of f^{-2} (where f is frequency). Below the inertial frequency, the kinetic energy frequency spectra has a range of energetic frequencies: inertial oscillations are observed as a broad peak around the inertial frequency, the M_2 lunar tide appears as a sharp peak, and a broadband internal wave continuum ranges between the inertial frequency and the buoyancy frequency. However, from *Ferrari*

and Wunsch [2009] not much information is available about frequency spectra on annual and longer periods, nor can we understand geographical variations in spectral characteristics.

In contrast to frequency spectra, only a few wavenumber estimates exists of ocean variability on global and on regional scales, essentially resulting from altimetric satellite data [e.g., *Le Traon and Rouquet*, 1990; *Stammer and Böning*, 1992; *Provost and Le Traon*, 1993; *Stammer*, 1997; *Le Traon et al.*, 2008; *Xu and Fu*, 2011, 2012]. SSH wavenumber spectra tend to be red without the distinctive features seen in the frequency domain, such as tidal peaks or inertial oscillations [*Ferrari and Wunsch,* 2009].

The geostrophic kinetic energy wavenumber spectrum can be retrieved from the SSH spectrum by multiplying it by k^2, where k is the wavenumber [*Stammer*, 1997], thereby giving the spectra a more "blue" character than visible in the SSH spectra, and at the same time enhancing the influence of remaining small-scale data noise in the altimetric estimates. *Stammer* [1997] therefore discussed the need to remove data noise from the along-track altimeter data prior to estimating spectral slopes from the resulting wavenumber spectra. Along these lines, *Xu and Fu* [2012] revealed that after removing the white noise level of altimetry, which was best estimated from the spectral values at wavelengths of 25–35 km, the spectral slope values changed significantly over most of the oceans.

Xu and Fu [2011] were able to show that after the attempt of a compression of small-scale noise, the resulting geographic pattern of spectral wavenumber slopes is similar to the regional pattern of eddy variability. The authors describe the geographical wavenumber slope pattern as showing steeper spectral slopes in the vicinity of higher eddy variability and less steep slopes elsewhere, suggestive of a link between a steep spectrum and nonlinear dynamics, while the flat spectrum might be associated with more linear dynamics. The authors further argued that the surface quasi-geostrophic theory can be used to explain the observed spectra only in the transition zones from the edge to the core of the high-energy regions of the major ocean current systems.

An important issue remains in the unknown level and spectral characteristics of noise in altimetric observations, especially below wavelengths of 100 km, leaving the question open whether we can understand existing altimetric SSH and slope spectra below spatial scales of 100 km in terms of underlying ocean dynamics or whether we have to ascribe observed variability on those spatial scales entirely to noise in the altimetric data. Because of this, we revisit here the problem of estimating frequency and wavenumber spectra and spectral relations from observations by taking stock of the 23 year long altimeter data set now available since 1993. The spectra, computed over the Atlantic Ocean, are then compared against those computed from the output of a hierarchy of ocean circulation simulations, run with spatial resolutions of 16, 8, and 4 km. Our rational for such a joint analysis is twofold: on the one hand it is important to test the quality of the model results, as a function of spatial resolution, against observations. On the other hand, such a comparison might also qualify to identify altimeter data errors and their spectral frequency and wavenumber relation. Although satellite altimetry provides the best available data set for the study of the ocean mesoscale variability from the observational point of view, ocean general circulation models increasingly expand and complement our understanding of physical processes underlying observed variability. As will be seen below, one clear advantage of models is the fact that they can be sampled with a daily rate (or better) as opposed to the 10 day sampling of altimetric data, thereby allowing to identify aliasing effects in altimetric results.

The remaining paper is structured as follows: section 2 provides a short description of the analyzed altimetric and model data. In section 3 resulting frequency spectra of SSH and surface geostrophic currents are discussed as basin averages and for distinct dynamical regions. A similar discussion, but for wavenumber spectra is provided in section 4. A final discussion and concluding remarks are provided in section 5.

2. Altimetric and Model Data

This study is based on 23 years of along-track altimetric SSH observations, available from 1993 to the end of 2015, as well as simulations available from a hierarchy of model experiments for the Atlantic and the Arctic Oceans. In the following, we will briefly describe both data sets.

2.1. The Altimetric Data Set

Sea surface height data from the global ocean topography experiment TOPEX/Poseidon, Jason-1 and Jason-2 (henceforth termed TPJJ) satellites were retrieved from the Radar Altimeter Database System (RADS, [*Scharroo*

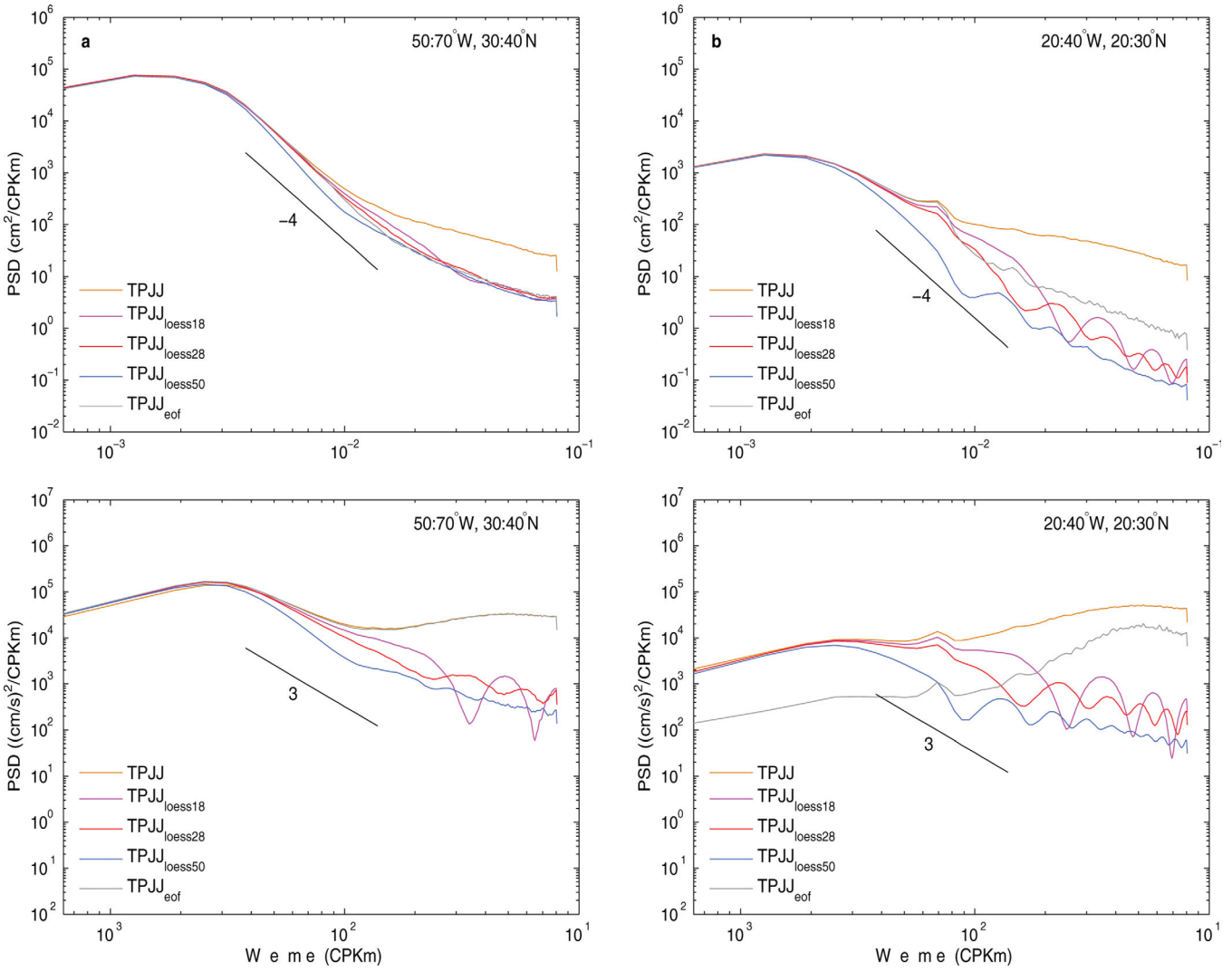

Figure 1. (a, b) Wavenumber spectra of sea surface height and (c, d) surface geostrophic velocity computed using different filters for regions b and c indicated in Figure 2.

et al., 2013, http://rads.tudelft.nl/rads/rads.shtml]) and further analyzed along-track without any mapping procedure involved. The horizontal along-track data resolution is 6.2 km and the temporal resolution is equal to the repeat period of 9.9156 days. We used along-track SSH data from 1 January 1993 to 31 December 2015, which were derived by combining repeat cycles 11–363 from TOPEX/Poseidon, 21–259 from Jason-1 and 21–276 from Jason-2, so as to produce a continuous 23 year long-time series. Typical corrections for environmental effects were applied to the data using information available on the Geophysical Data Records [*Scharroo et al.*, 2013]. In particular, corrections accounting for the effects of the atmospheric loading, the ionosphere, the wet and dry troposphere, the geophysical tides, and the atmospheric dynamics were applied.

The altimeter data were interpolated along-track in space and at each along-track position also in time whenever gaps were smaller than 20 days and 30 km; larger gaps remained unfilled. Finally, a 23 year temporal mean was subtracted from each SSH measurement, to produce time series of SSH anomaly which formed the basis for the remaining analysis. To reduce noise in the SSH anomalies, an along-track spatial Loess filter was applied following [*Scharffenberg and Stammer*, 2010, and reference therein], with a latitudinal dependence according to $L(\phi) = \frac{28\,\mathrm{km}}{|sin(\phi)|}$ (ϕ being the geographic latitude). The following analysis is built exclusively on the filtered altimetric anomalies (henceforth called $TPJJ_{loess}$).

Other choices of filters exist and have been applied. As an example, *Zhou et al.* [2015] used an EOF decomposition to filter data in space and time by keeping only the gravest modes in the analysis. As demonstrated

in Figure 1, the Loess filter with 28 km filter length scale appears as a good compromise since it does not seem to oversmooth the spectra (like the 50 km filter) and does not introduce unwanted artifacts (like the 18 km version) especially in low-energy regions. On the other hand, applying the Loess filter with nominal wavelength of 28 km seems to be as effective as an EOF filter approach, but possesses a well-defined transfer function. The choice of a 28 km filter length is consistent with the findings of *Xu and Fu* [2012], who argued that the variability level in the wavelengths band 25–35 km is a good representation of the data noise.

From the filtered SSH anomalies, the geostrophic cross-track surface velocity anomaly, v_g, was computed (also relative to a 23 year mean) according to:

$$v_g = -\frac{g}{f}\frac{\partial \zeta}{\partial l}. \quad (1)$$

Here ζ stands for the filtered SSH anomaly, $TPJJ_{loess}$, g is the Earth gravity, $f = 2\Omega\sin(\phi)$ is the Coriolis parameter, Ω is the Earth angular velocity, and ϕ is the geographic latitude. l represents the along-track coordinate (positive northwards).

2.2. Atlantic Ocean Simulations

To complement the analysis of the altimetric SSH observations, we use results from three different integrations of the MIT general circulation model [*Marshall et al.*, 1997] covering the Arctic Ocean and the Atlantic Ocean north of 33°S, together featuring a hierarchy of horizontal resolutions: 16, 8, and 4 km (henceforth termed ATL simulations). In each case, the model was set up with a bipolar curvilinear grid, with one pole located over North America and the other over Europe. In the vertical, all model setups use 50 levels (16 km and 8 km models) or 100 levels (4 km model) of varying depth, from 10 m (16 km and 8 km models) and 5 m (4 km model) in the upper ocean to 456 m (16 km and 8 km model) and to 185 m (4 km model) in the deep ocean. Bottom topography is derived from the ETOPO 2 min resolution database. The initial conditions are derived from the annual mean temperature and salinity from the World Ocean Atlas 2005 [*Boyer et al.*, 2005] in the case of the 16 km and 8 km models. The 4 km model starts from the year 2002 conditions from the 8 km model. The vertical mixing parametrization employed in the simulations uses the KPP formulation. Background coefficients of vertical diffusion are set to $10^{-5}m^2s^{-1}$ and of vertical viscosity to $10^{-4}m^2s^{-1}$. Horizontally, biharmonic diffusion and viscosity represent unresolved eddy mixing, with coefficients of horizontal diffusion and viscosity set to $1 \times 10^{10}\, m^4s^{-1}$ (16 km model), $5 \times 10^9\, m^4s^{-1}$ (8 km model), and $1 \times 10^9\, m^4s^{-1}$ (4 km model).

All model simulations are forced at the surface by fluxes of momentum, heat, and freshwater computed using bulk formulae and either the 1948–2009 6 hourly atmospheric state from the NCEP RA1 reanalysis [*Kalnay et al.*, 1996] (for the 16 km and 8 km resolutions) or the 1989–2009 ECMWF ERA-Interim reanalysis [*Dee et al.*, 2011] (4 km resolution). At the open southern boundary, the simulations are forced by the output of a 1° resolution global solution of the MITgcm forced by the NCEP data set. A barotropic net inflow of 0.9 Sv ($1\ Sv = 10^6\, m^3s^{-1}$) into the Arctic is prescribed at Bering Strait, the models' northern open boundary, which balances a corresponding outflow through the southern boundary at 33°S. An annually averaged river run-off is applied at river mouths and a dynamic thermodynamic sea ice model solves for sea ice parameters. Details about the model performance and detailed validations against observations can be found in *Serra et al.* [2010], *Köhl and Serra* [2014], *Koldunov et al.* [2014], and *Sena Martins et al.* [2015]. In the present work, we use daily averaged model SSH fields, spanning the period from 1990 to 2002 for the run with resolution of 16 km, from 2003 to 2009 for the 8 km resolution run, and from 2003 to 2009 for the 4 km resolution run.

The Eddy Kinetic Energy (EKE) field derived from the ATL different resolution outputs is shown in Figure 2, attesting the high degree of realism of the 4 km resolution simulation concerning patterns of variability relative to altimetry. The improvement above the 8 km simulation is especially obvious in the so-called Northwest Corner of the North Atlantic and along the Azores front. It is also obvious from the basin-averaged variability levels, which result in 90.3, 71.8, and 46.8 cm^2s^{-2} for the 4, 8, and 16 km simulations, respectively. Nevertheless, as compared to the altimetric estimate (121.2 cm^2s^{-2}), the 4 km simulation still remains low by a factor of 1.34. This deficiency is most obvious in low latitudes (factor of 2 too low), while in mid and high latitudes the agreement is more favorable. It is interesting to note that in the eastern Atlantic, high

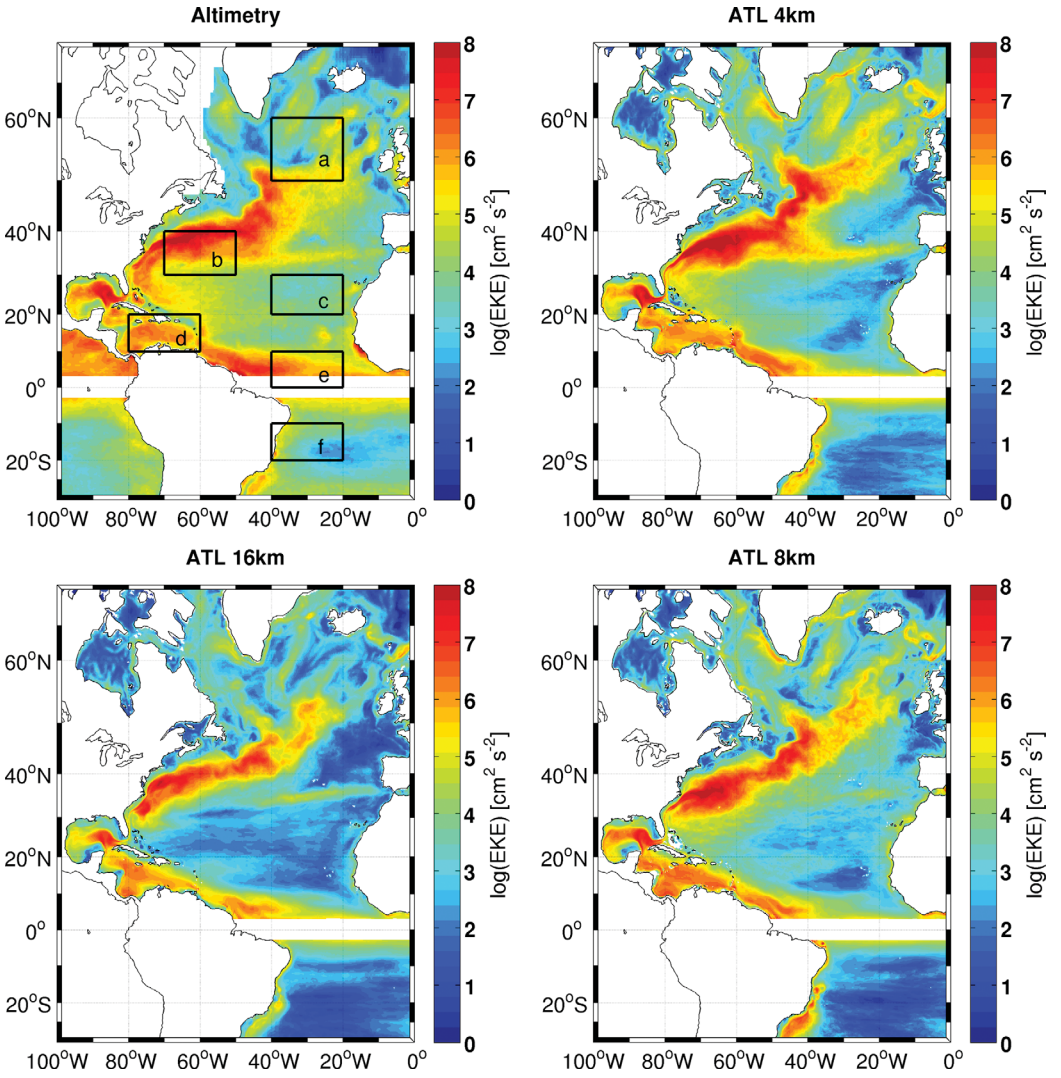

Figure 2. Eddy Kinetic Energy (in logarithmic scale) from altimetry and ATL simulations with different resolutions. The boxes indicate the regions for which regional spectra were computed and are presented in Figures 4, 6, 9, and 11.

levels of energy occur downstream of island chains, but are absent in the model simulations. This suggests the need for high-frequency and also high spatial resolution in the wind forcing fields, since they are needed to correctly simulate the forced flow past topographic obstacles.

To be comparable with the results obtained from the altimeter data, model SSH fields were interpolated onto the altimetric along-track arcs before data were further processed in form of frequency and wavenumber spectra. From interpolated model SSH fields, geostrophic velocities were computed similarly to the procedure used in the altimeter data processing. In addition, the data from the 4 km model were resampled every 10 days in order to compare daily sampling against the altimeter type of sampling.

3. Frequency Spectra

Frequency spectra of SSH anomalies and respective surface geostrophic velocity anomalies were computed using a Hamming windowed Fast Fourier Transformation (FFT) approach applied over the full length of the available data—either for a full basin or over subregions. At each along-track position, any remaining temporal trend was removed from each data set prior to computing the frequency spectra, which were averaged subsequently over larger regions as specified below. To avoid equatorial singularities in velocity estimates, data

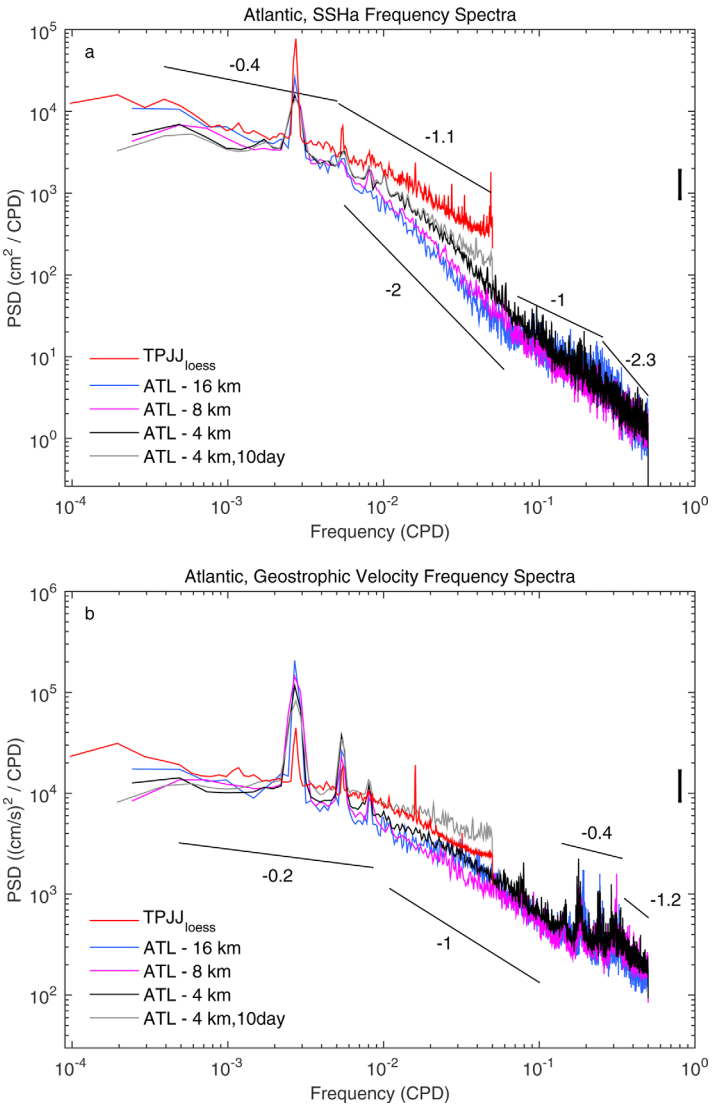

Figure 3. Atlantic Ocean (100°W to 0° and 30°S to 70°N) averaged (a) sea surface height and (b) surface geostrophic velocity frequency spectra from filtered altimetry data (TPJJ$_{loess}$—red) and from simulations with different resolutions (ATL—blue, magenta, and black), including 10 day resampled data from the 4 km model (grey). The vertical line on the right side of the spectra corresponds to the 95% confidence interval.

located between 4°S and 4°N were excluded from further analysis and do not enter any frequency or wavenumber spectrum.

3.1. SSH Spectra

Basin-averaged SSH frequency spectra, computed from TPJJ$_{loess}$ and from ATL simulations for the Atlantic Ocean between 100°W and 0° and between 30°S and 70°N are shown in Figure 3a. The TPJJ$_{loess}$ frequency spectrum available between frequencies of $1/(10^4 \text{ days}) < f < 1/(20 \text{ days})$ follows a spectral relation close to $f^{-0.4}$ at periods longer than about 200 days. For periods shorter than 200 days, the spectral relation is close to $f^{-1.1}$. Only toward the altimetric Nyquist frequency of about 1/(20 days) the spectrum seems to indicate a slight flattening. We note that, in overall terms, those power laws are close to the ones obtained from a global averaged altimeter spectrum (not shown).

Superimposed to the continuous altimetric spectrum are peaks associated with the seasonal cycle of SSH and its higher harmonics. On periods shorter than 100 days, the spectrum depicts in addition residual tidal aliasing peaks, notably at the aliased M_2 (62.1 days), S_2 (58.7 days), as well as O_1 (45.7 days) and M_4 (31.1 days) periods [*Ray*, 1998]. Other peaks appear close to the aliased MSf (30.2 days), M_1 (23.6 days), $2N_2$ (22.5 days), M_6 (20.7 days), and μ_2 (20.3 days) periods.

On periods longer than 100 days, the shape of the spectra simulated by the hierarchy of models is similar to the altimetric result, albeit resulting in slightly lower-energy levels. However, on periods shorter than about 180 days, all model spectra follow a substantially steeper spectral slope close to f^{-2}. Since the model results are available as daily averages, they resolve frequencies down to a Nyquist cut-off of 1/(2 days). On frequencies between 1/week and 1/(5 days), model slopes flatten roughly to a f^{-1} relation, but become steeper again at higher frequencies. Peaks in the ATL 4 km spectrum on subseasonal periods represent higher harmonics of the annual cycle.

Comparing the basin-averaged model frequency spectra obtained with different resolutions, we find similar spectral shapes on long and short periods; however, with increasing resolution the model energy levels come closer to the observed altimetric level within an intermediate frequency range. Nevertheless, a clear wedge of unresolved energy levels in the model results persists between periods of 20 and 100 days, even with a nominal model

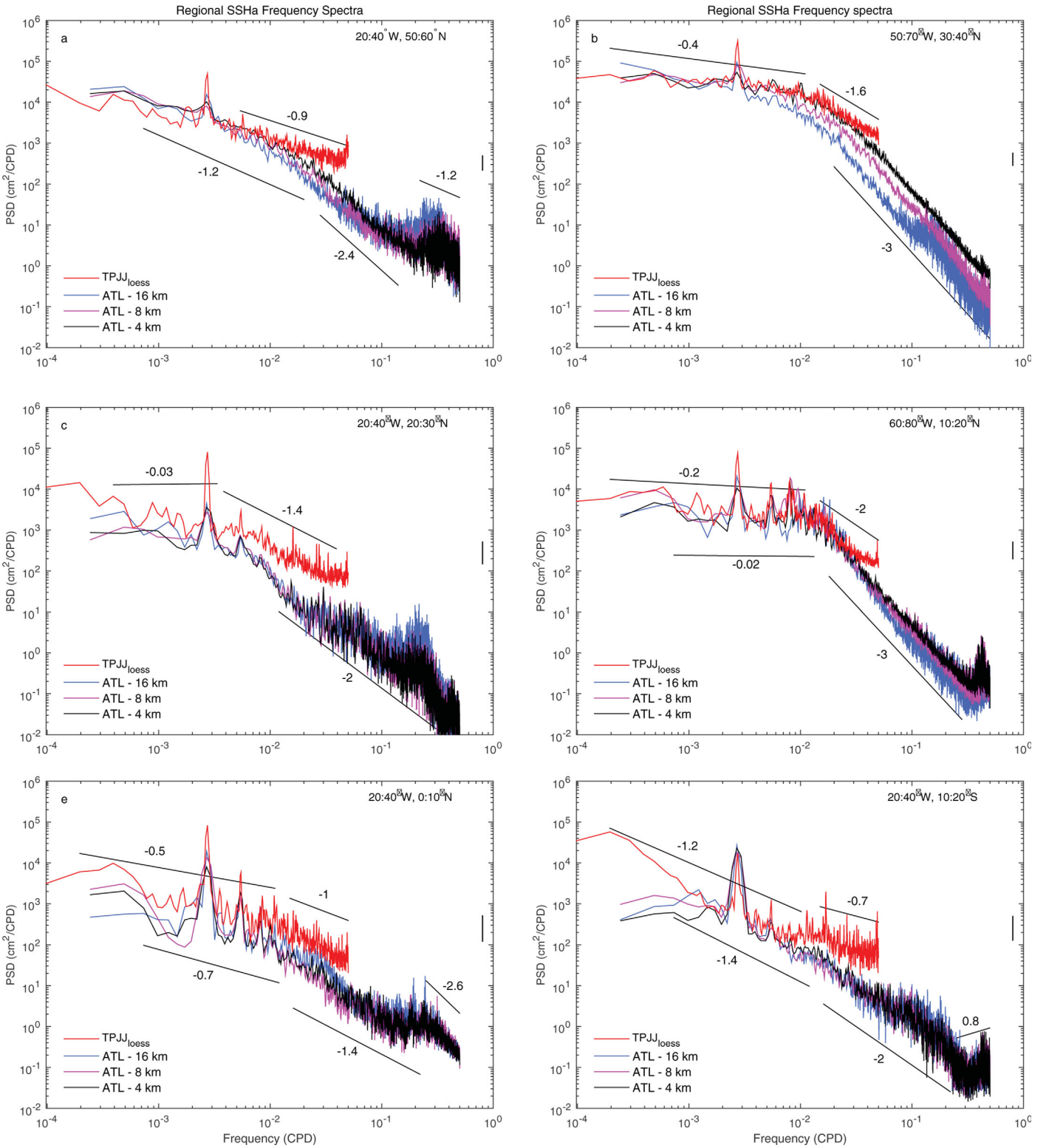

Figure 4. Sea surface height frequency spectra from TPJJ$_{loess}$ altimetry data (red) and ATL simulations with different resolutions (blue, magenta, and black), averaged in specific dynamically different regions (see Figure 2 for the region's location). The vertical line on the right side of the spectra corresponds to the 95% confidence interval.

resolution of 4 km. The reason for the inconsistency with altimetry could be either related to the fact that even a model with 4 km horizontal resolution is lacking the ability to properly describe submesoscale phenomena or that the altimetry spectra is dominated by noise at these frequencies. It is likely that both effects are involved.

Table 1. Frequency Spectral Slopes in Specific Period Bands From ATL Simulations With Different Resolutions[a]

Slopes of SSH Frequency Spectra						
	(16 km, 8 km, 4 km)					
Period (days)	Region a	Region b	Region c	Region d	Region e	Region f
5–62	−1.3, −1.7, −2.3	−2.6, −2.9, −2.9	−0.9, −1.5, −1.6	−3.2, −3, −3	−1.5, −1.2, −1.5	−1.4, −1.7, −1.8
90–140	−1.6, −1.5, −2.1	−1.5, −1.7, −0.3	−3, −2.4, −2.9	3, −2, −1.3	−0.6, −1.3, −0.2	−1.7, −1.2, −0.4
Slopes of Geostrophic Velocity Frequency Spectra						
	(16 km, 8 km, 4 km)					
Period (days)	Region a	Region b	Region c	Region d	Region e	Region f
2–20	−2.3, −3, −2.9	−4.2, −2.9, −2.6	−2.8, −1.9, −3	−2.6, −2.5, −2.2	−0.6, −0.2, −0.4	−1.6, −2.2, −2.3
186–1024	−0.6, −0.6, −0.4	−0.5, −0.2, −0.2	−0.3, −0.5, −0.4	−0.05, −0.04, 0.1	0.07, 0.4, 0.4	−0.9, −0.8, −0.5

[a]The studied regions are defined in Figure 2.

As a third cause, we note that the frequency spectrum derived from the 10 day resampled 4 km model data follows closer the altimeter spectrum, indicating that some fraction of the altimetric spectra likely displays too high an energy level at the high-frequency end simply due to aliasing of unresolved energy, with a severity that depends on the geographic position. Because no full high-frequency wind stress or pressure forcing is invoked in the model runs since only 6 hourly wind stress forcing is applied, in reality the aliasing might be even more significant. Respective aliasing effects can be expected to impact the altimetric estimate especially in high latitudes, and along all frontal axes, where fast barotropic motions are pronounced. Enhanced aliasing might also appear close to the equator where again enhanced fast motions exists.

To illustrate the variation of frequency spectra representing different dynamic regimes, thereby also illustrating the geographic dependence of the fidelity of the model simulations, we show in Figure 4 SSH frequency spectra from altimetry and all model simulations for selected 20° × 10° (longitude by latitude) regions (see also Table 1 for additional spectral slopes and Figure 2 for the location of the regions). The figure illustrates that in several regions the model results are in very good agreement with the observed variability levels, especially northward of 30°N and at frequencies shorter than roughly 1/(60 days). This holds for the model resolution of 4 km, but not so much for the 8 km resolution, underscoring the need for model resolutions of 4 km or higher resolution. The agreement is especially good in western boundary current regions and in subtropical and subpolar latitudes (Figures 4a, 4b, and 4d); it is less obvious in less variable regions at latitudes south of 30°N (Figures 4c, 4e, and 4f), where all model results underrepresent the observed variance over the entire frequency range. We note that Figure 4d displays a unique frequency spectral shape relative to the other selected regions (flat for periods longer than 75 days and following f^{-3} for periods shorter than 75 days). Some other regions also display a fairly white long-period spectrum, while other regions show a f^{-1} long-period slope. Moreover, model results reveal enhanced variability on the 2–5 day band. This holds especially in the subpolar area, and in the tropical to subtropical bands, both regions of enhanced wind forcing variability with respective time scales.

It is obvious from Figure 4 that the shape of the presented frequency spectra depends on latitude, regional energy level and, in the case of the model, the resolution. To illustrate the full details of the geographic variations, SSH frequency spectra are shown in Figure 5 as weighted averages over 20° × 20° (in latitude and longitude) boxes. In the figure, altimetric results are compared only with those available from the 4 km model solution. As before, the model frequency spectra appear steeper than those from altimetry at high frequencies. However, energy levels tend to agree very well on periods longer than a cut-off frequency of approximately 1/(100 days); in detail, this cut-off is a function of latitude and dynamical regime. The best agreement can be found in high latitudes and in regions of highest SSH variance such as the Gulf Stream and its extension across the North Atlantic (the North Atlantic Current, NAC), where mesoscale eddies dominate other contributions to the spectra. We also recall that the best agreement between altimetry and ATL simulations was found for the resolution of 4 km, a fact that is even more obvious in the velocity spectra shown below.

It appears that both spectral estimates show clear seasonal and subseasonal peaks as they are to be expected for sea level. In the tropics, the semiannual frequency peak becomes even more pronounced in

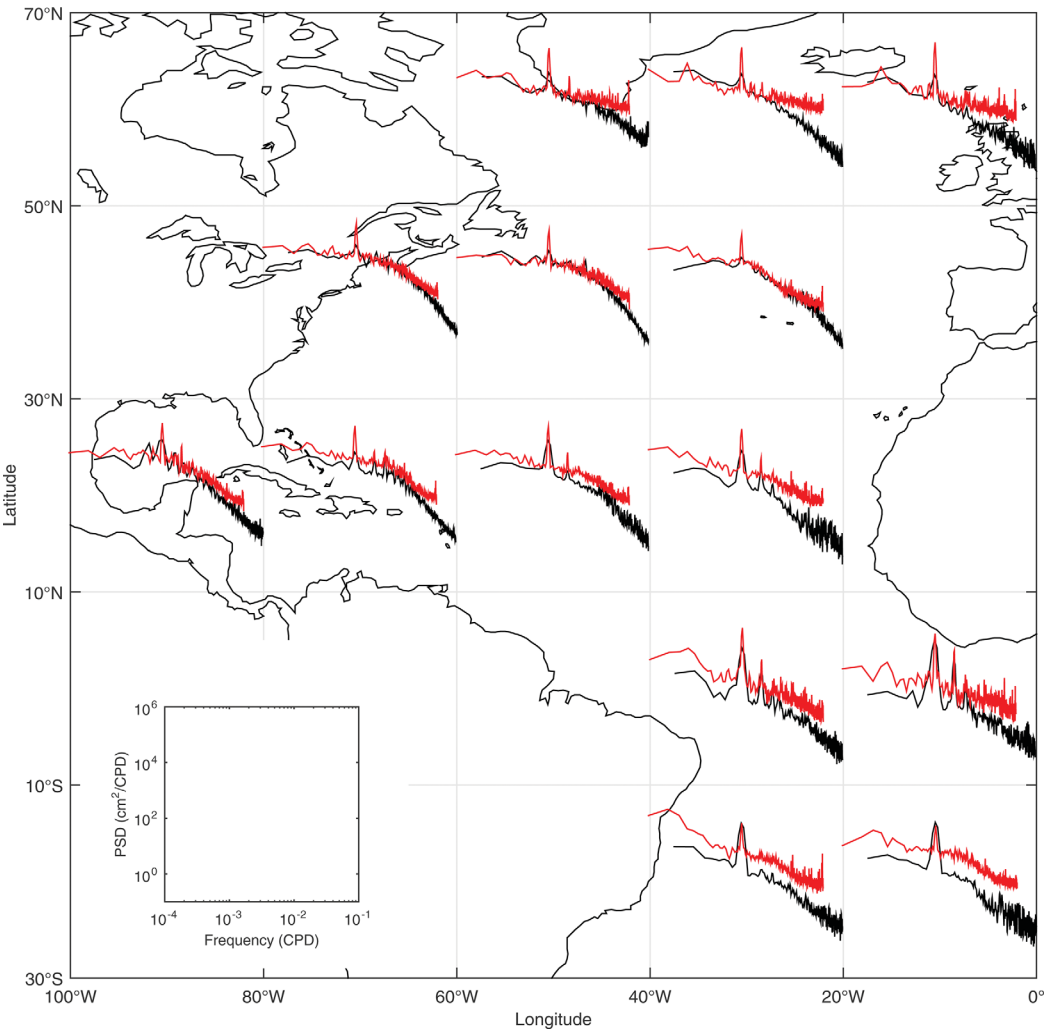

Figure 5. Sea surface height frequency spectra from $TPJJ_{loess}$ altimetry data (red) and from the ATL simulation with 4 km resolution (black) averaged over 20° × 20° grid boxes.

the model's frequency spectra, indicating the dominance of the seasonal cycle there. In addition, the altimeter curves show peaks at tidal aliasing frequencies. Similar peaks in low latitudes could represent additional variability not related to tides, such as basin modes [e.g., *Cane and Moore,* 1981; *Jin*, 2001]. We also note that all peaks in the altimetric spectra on higher than subseasonal frequencies are more prominent along the eastern basin due to the complexity of the tidal dynamics as well as the dynamic response to pressure forcing there [*Ponte and Lyard*, 2002].

3.2. Geostrophic Velocity Spectra

Basin-averaged frequency spectra for the geostrophic velocity are shown in Figure 3b, as they follow from the filtered altimeter data and the hierarchy of model runs. The basin-averaged altimetric velocity spectrum (again taking into account the relative regional representation of individual spectra; see above) is in good agreement with model results with respect to its shape, but shows higher energy levels. Down to about 1/(100 days), the model velocity spectra closely follow a $f^{-0.2}$ relation roughly at a similar energy level; at higher frequencies, up to about 1/(8 days), the models spectral energy closely follows a f^{-1} relation, but becomes flat at even higher frequencies where several peaks become prominent at frequencies of 1/(5.6 days), 1/(4 days), and 1/(3 days). Over frequencies above 1/(3 days), the spectral decay increases again to $f^{-1.2}$. For periods shorter than 200 days, the altimetric frequency spectrum follows a $f^{-0.8}$ slope; a slope of $f^{-0.6}$ was found for the spectra derived from the 10 day resampled 4 km model fields. Peaks found in the model frequency spectra, to first order, are aligned with the annual period and its higher harmonics at 6 month and 3 month periods. We note that at

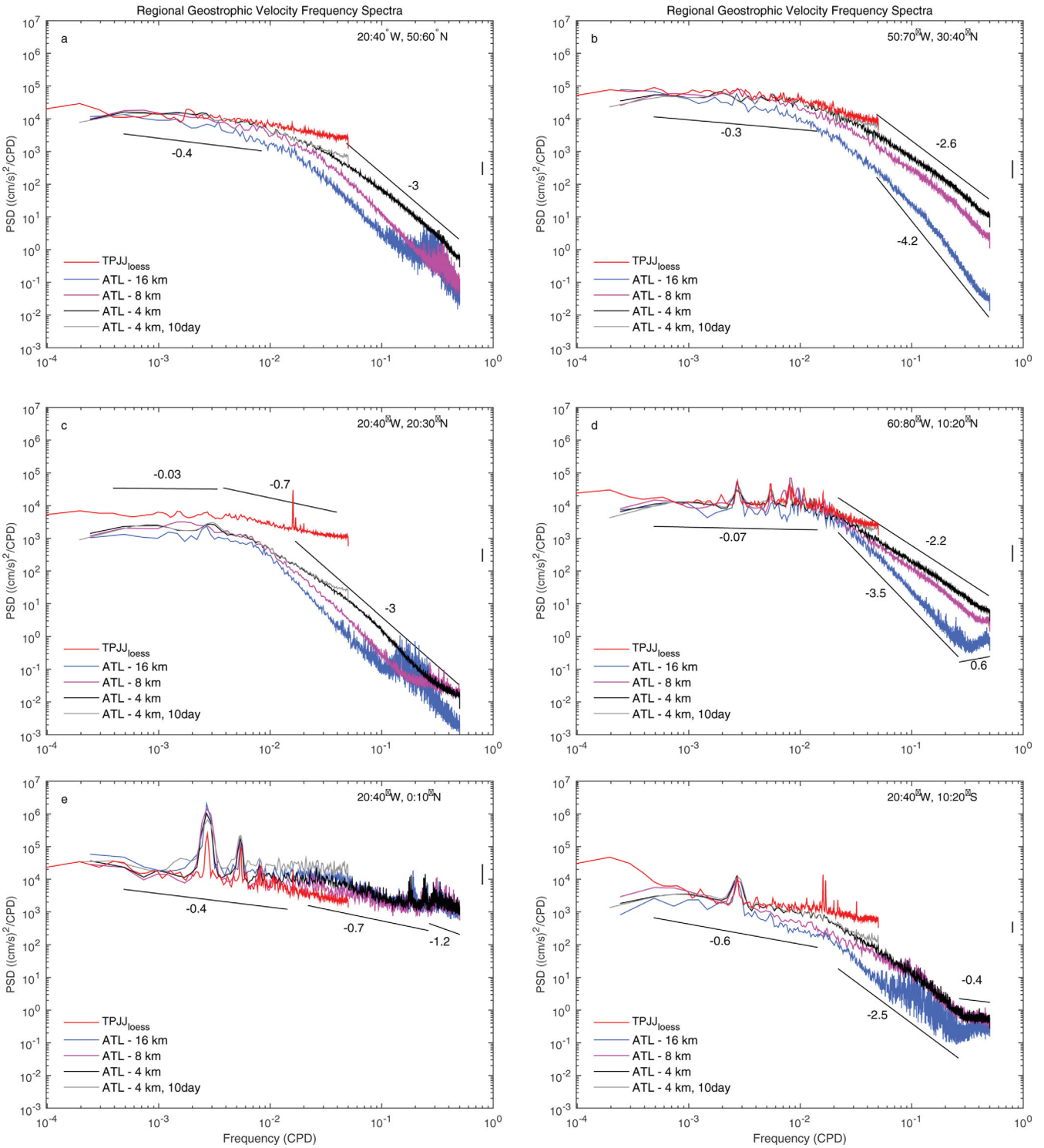

Figure 6. Surface geostrophic velocity frequency spectra from $TPJJ_{loess}$ altimetry data (red), from ATL simulations with different resolutions (blue, magenta, and black) and from 10 day resampled 4 km model data (grey), averaged in specific dynamically different regions (see Figure 2 for the region's location). The vertical line on the right side of the spectra corresponds to the 95% confidence interval.

those periods the altimetric result also shows increased energy; however, the peak around 1/(60 days) in the altimeter spectrum coincides with the M_2 tidal aliasing frequency.

While an aliasing effect from the unresolved variability was already identified for periods shorter than 100 days in the basin-averaged SSH frequency spectrum, this effect is much more visible in the basin-averaged velocity

frequency spectrum, for which the aliased model curve from the 10 day resampled 4 km model is now statistically similar to the altimetric variability levels on periods shorter than 50 days. This suggests that the altimetric velocity spectra are heavily aliased and show too much energy on its high-frequency end, presumably all the way to the annual cycle. The reason that velocity spectra are much more affected by aliasing than SSH spectra is related to the fact that velocities show much more energy on periods shorter than 10 days associated with lower spectral slopes. As will become clear below (Figure 6), most of that high-frequency energy comes from the tropical Atlantic; in contrast mid and high-latitude regions are less affected.

Altimetric and ATL model velocity spectra from selected 20° × 10° (longitude by latitude) areas representing different dynamical regimes are shown in Figure 6 (see also Table 1 for spectral slopes and Figure 2 for the location of the regions). The altimetric spectral slopes are flat, particularly in the low-energetic regions (ranging from $f^{-0.1}$ to $f^{-0.7}$) than the high-energy regions. The figure reveals that the model also produces a flat spectrum at periods longer than about 100 days, but leads to a steeper decay toward short periods. However, the frequency at which the spectrum turns from flat to steep tends to shift toward shorter periods in low latitudes as compared to high latitudes. This finding is consistent with *Müller and Frankignoul* [1981], who inferred a theoretical frequency spectrum resulting from an atmospheric forcing response of a quasi-geostrophic ocean. Their hypothetical spectrum of the ocean is white at low frequencies. It changes smoothly to an f^{-2} power law at a frequency $f=\beta L_D/2$, where L_D is the first baroclinic mode deformation radius and $\beta=\frac{\partial f}{\partial y}$. The frequency at which the transition occurs should decrease toward lower latitudes through its dependance on L_D. Along those lines, *Wortham and Wunsch* [2014] found a low-frequency energy plateau in kinetic energy frequency spectra computed from moored current meter data in the North Pacific, with an overall transitioning to a high-frequency f^{-2} power law; the break point between the low-frequency white spectrum and the f^{-2} power law decreased with latitude similar to what we find in the altimetric results. The authors found dominant periods increasing from approximately 100 days near the equator to around 300 days at 40°N. Similar to SSH frequency spectra, model velocity frequency spectra also display enhanced variability in the 2–5 day band for the subpolar and tropical-subtropical bands.

A deviation from the general behavior described above appears to hold in the tropical latitude band ± 10° (where the model spectra are generally white) superimposed by several peaks. Again most noticeable are the annual and semiannual frequencies; however, the spectrum at higher frequencies appears generally more noisy. Strong variability in the geostrophic velocity spectra is visible specifically in the western tropical Atlantic (Figure 6e), where three peaks at the lower frequencies of 1/(372 days), 1/(186 days), and 1/(120 days) are present and where another three peaks at higher frequencies, namely, 1/(5 days), 1/(4 days), and 1/(3.4 days) are visible indicating the strong effect of the wind forcing in this region. We also note that the latter three frequencies are consistent with eigenmodes in the tropical Atlantic.

Velocity spectra clearly demonstrate the need for high spatial model resolution. This holds especially in high latitudes, where even upon the increase of the model resolution from 8 to 4 km, a substantial increase in the simulated variance is obvious on periods roughly shorter than 2 months, thereby bringing the model results significantly closer to the observed altimetric energy levels. In contrast, all model results tend to agree near the equator, where especially the 8 km run is very close to the 4 km run over the frequencies shown.

Arbic et al. [2012] computed frequency spectra of kinetic energy from AVISO gridded satellite altimeter data and showed that some regions are dominated by an "inverse temporal cascade," while other regions exhibit a "forward temporal cascade." The authors noted that spectral flux computations are highly susceptible to the smoothing inherent in the construction of gridded altimeter products. This was the first attempt to address quasi-geostrophic turbulence in the frequency domain. In high-energy regions, the ATL spectral slopes shown in Figure 6 are close to the estimates of *Arbic et al.* [2012]. The authors reported that realistic ocean models exhibit steeper slopes at higher frequencies and flatter slopes at lower frequencies and suggested that nonlinearities drive energy to longer-time scales. *Arbic et al.* [2014] show a slope of f^{-2} for the frequency spectra of kinetic energy integrated over all wavenumbers, as suggested by the energy cascade in frequency space. They also find spectral slopes around $f^{-1.6}$ and $f^{-2.1}$ for the 14–68 day periods in different regions. *Callies and Ferrari* [2013] suggest that f^{-2} spectral slopes in kinetic energy frequency spectra can be associated with various unbalanced processes like internal tides, and that ageostrophic flows may be important near the surface in regions of weak mesoscale eddy activity.

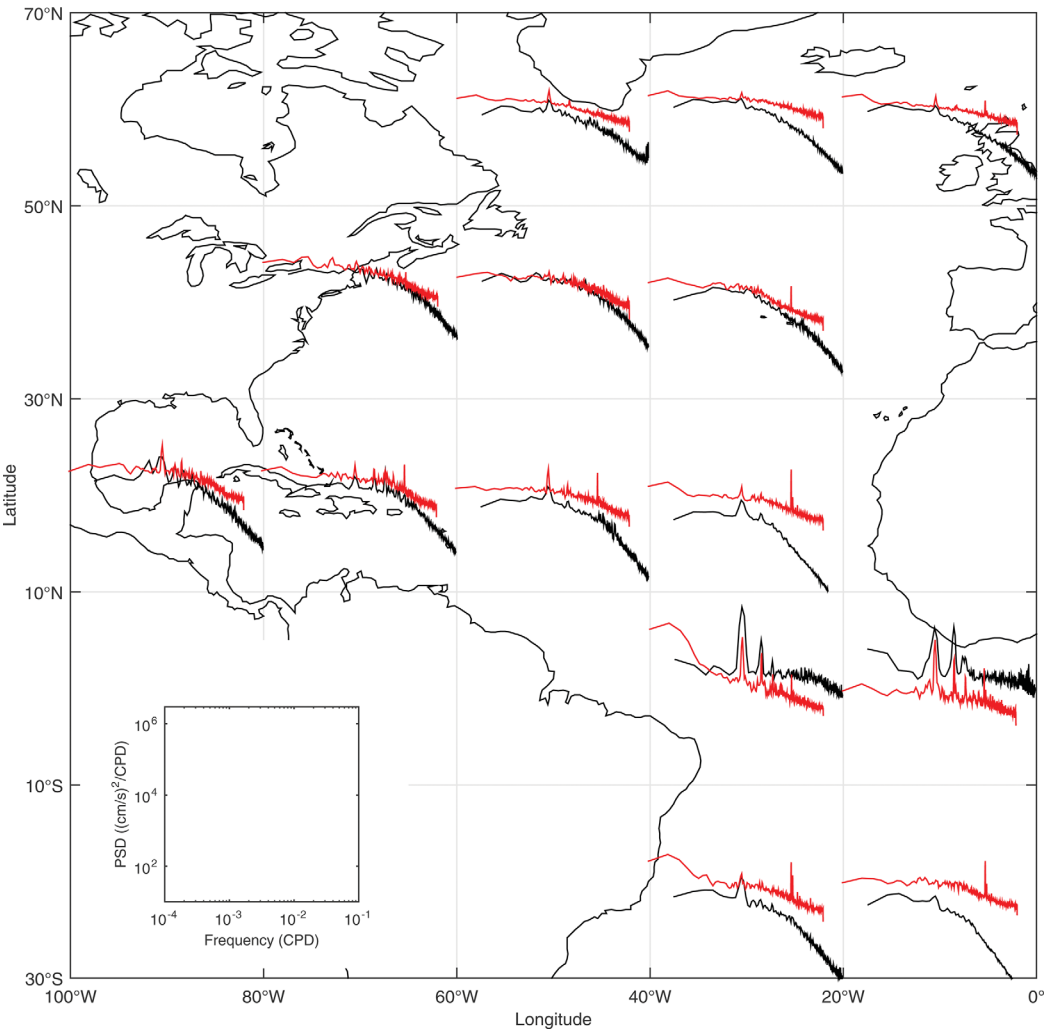

Figure 7. Surface geostrophic velocity frequency spectra from TPJJ$_{loess}$ altimetry data (red) and from the ATL simulation with 4 km resolution (black) averaged over 20° × 20° grid boxes.

To provide an overview of how velocity frequency spectra vary over the entire basin, thereby expanding on the comparison of the 4 km model results with the altimetric results, we show in Figure 7 a comparison between altimetry and ATL 4 km in 20° × 20° (in longitude by latitude) subregions across the entire basin. The altimeter spectra follow closely the ATL 4 km results especially in the zonal band between 30°N and 50°N, where even similar variance levels are being simulated by the model (taking into account aliasing problems in the altimetry). A clear lack of energy at the high-frequency end of the spectrum is obvious especially in the eastern subtropics and in the subpolar basin.

Contrary to SSH spectra, velocity spectra show no seasonal cycle over much of the Atlantic. However, in the tropical band both altimetry and model simulations show a pronounced variability on the annual period and its higher harmonics. The annual cycle is still present—albeit with much less prominence—in the subtropical region and also shows up in the subpolar band. However, it is especially the tropical variability that leads to the clear seasonal cycle present in the basin-averaged velocity frequency spectrum (Figure 3b). We note that this peak is missing in the previous results presented by *Ferrari and Wunsch* [2009], since it was based on shorter-time series and in addition represented midlatitude situations.

4. Wavenumber Spectra

Wavenumber spectra were computed from the along-track SSH anomaly and corresponding geostrophic velocity anomaly data over longitude-latitude areas of 20° × 20° and 10° × 10°, following the

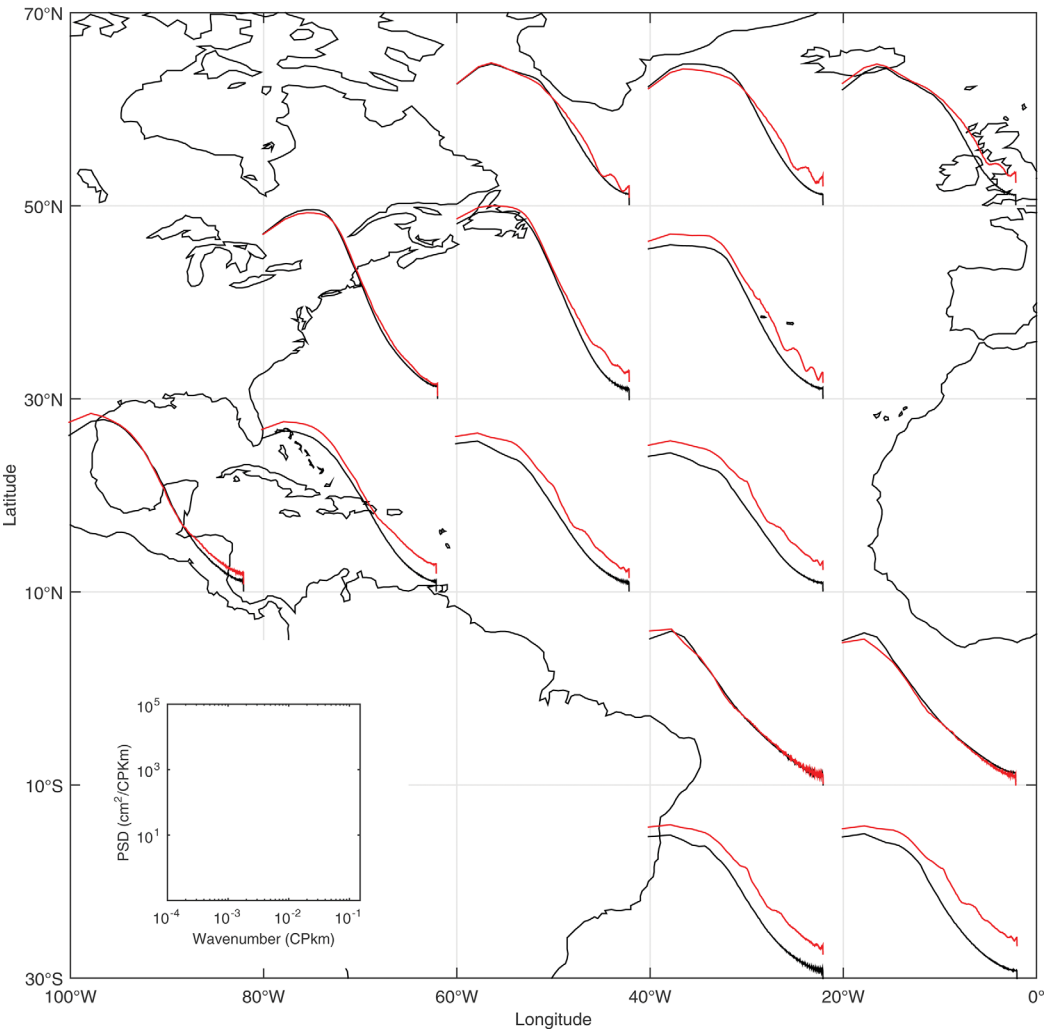

Figure 8. Sea surface height wavenumber spectra from TPJJ$_{loess}$ altimetry data (red) and from the ATL simulation with 4 km resolution (black) averaged over 20° × 20° grid boxes.

approach described by *Scharffenberg and Stammer* [2011]. In detail, between 30°S and 66°N, each arc was divided into segments each spanning 20° (or 10°) in latitude. Because satellite ground tracks are curved toward the turning latitudes, arc segments spanning 20° (or 10°) in latitude vary in their number of data points. To make wavenumber spectra compatible with each other, in each box the longest possible arc segment was chosen as a reference and all shorter segments were zero-padded to that length. For each arc and repeat cycle, the respective data were demeaned and detrended before wavenumber power spectra were computed using the FFT method. In each box, all resulting wavenumber spectra were averaged subsequently into one representative power spectral density estimate with the degrees of freedom and respective confidence levels of the spectrum depending on the number of arcs and repeat cycles being used in the averaging process. Typically the number of independent spectral estimates forming the base for the box mean spectrum is of the order of 14,700.

4.1. SSH Spectra

Previous studies revealed a clear latitudinal dependence in altimetric SSH and geostrophic velocity wavenumber spectra [see, e.g., *Stammer*, 1997; *Scharffenberg and Stammer*, 2011], therefore showing that basin-averaged wavenumber spectra is not meaningful. Instead we show in Figure 8 the altimetric wavenumber SSH spectra and the equivalent from the 4 km model simulation as averages over 20° × 20° (in longitude by latitude) subregions of the Atlantic. As can be seen from the figure,

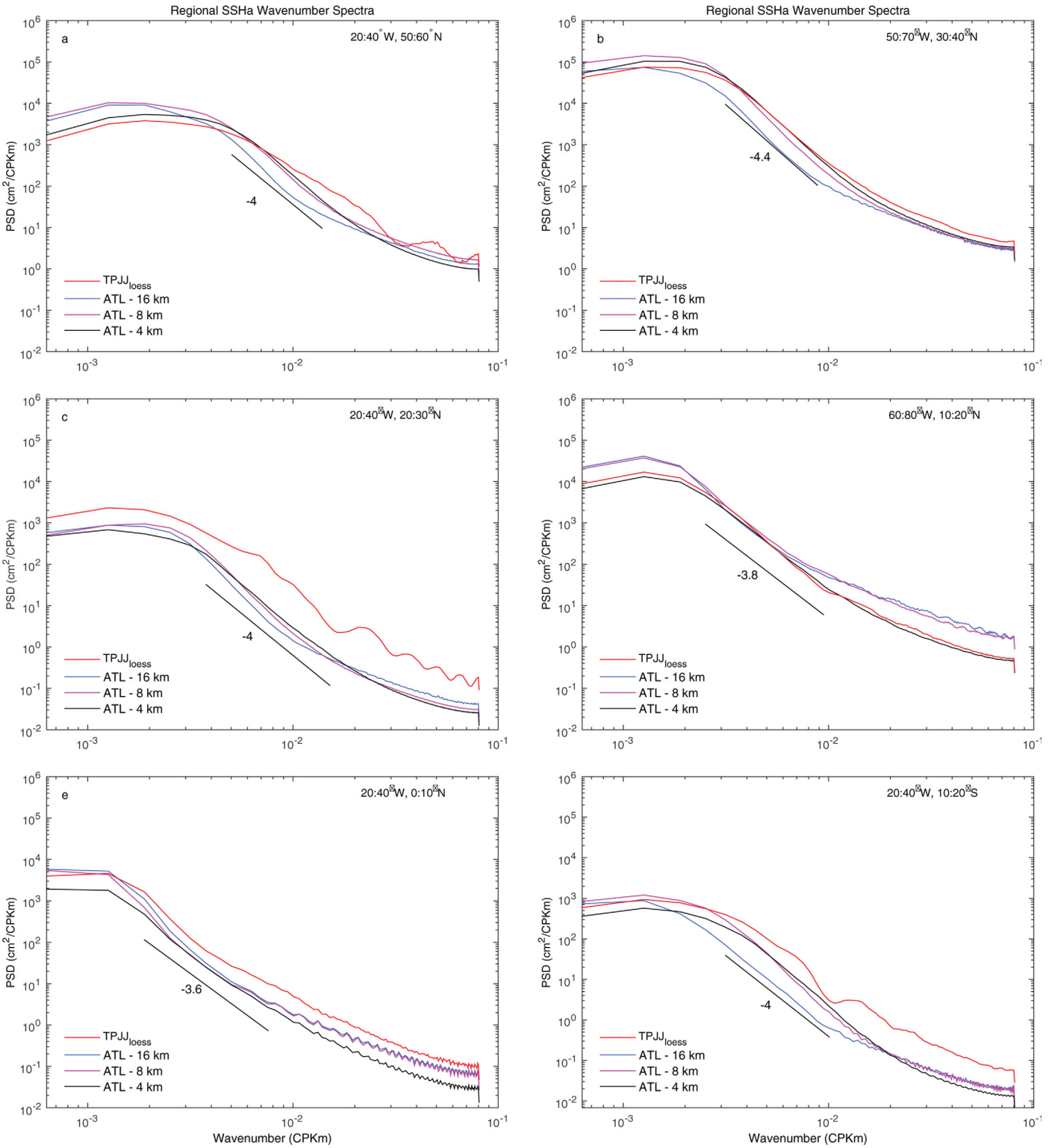

Figure 9. Sea surface height wavenumber spectra from $TPJJ_{loess}$ altimetry data (red) and ATL simulations with different resolutions (blue, magenta, and black), averaged in specific dynamically different regions (see Figure 2 for the region's location). The shown spectral slopes are fitted to the 4 km model.

the model agrees with altimetry surprisingly well in terms of amplitude and shape of the wavenumber spectra on long wavelengths and down to wavelengths between 100 and 250 km, depending on the latitude.

Table 2. Wavenumber Spectral Slopes in Specific Wavelength Bands From $TPJJ_{loess}$ and ATL Simulations With Different Resolutions[a]

Slopes of SSH Wavenumber Spectra					
($TPJJ_{loess}$ 16 km, 8 km, 4 km)					
Wavelength Range					
Region a	Region b	Region c	Region d	Region e	Region f
−2.7, −4.1, −4, −3.7	−4, −3.7, −4.4, −4.3	−3.7, −4, −4.4, −4	−3.6, −2.5, −2.8, −3.6	−2.6, −2.5, −2.4, −3	−4, −3.6, −4.6, −4.3
			70–250 km		
−3, −4.2, −4.2, −4	−4.1, −4.6, −4.8, −4.4	−3.8, −4, −4.4, −4	−4.2, −3.5, −3.6, −3.8	−3.5, −4, −3.6, −3.6	−4.1, −4.1, −4.6, −4
70–200 km	110–320 km	66–270 km	100–400 km	130–530 km	100–320 km
Slopes Of Geostrophic Velocity Wavenumber Spectra					
($TPJJ_{loess}$ 16 km, 8 km, 4 km)					
Wavelength Range					
Region a	Region b	Region c	Region d	Region e	Region f
−1, −4, −2.5, −2	−2.5, −3.7, −3.2, −2.7	−2, −4.5, −3.2, −2.4	−2, −3.7, −2.6, −2.4	−1, −1.6, −1.3, −1.3	−2.1, −4.6, −3, −2.5
			70–250 km		
−1.4, −4.5, −3.8, −3	−2.5, −3.5, −3.4, −2.9	−1.5, −3.6, −3.7, −2.8	−1.9, −3.6, −2.7, −2.4	−1.2, −1.5, −1.4, −1.4	−1.3, −3.6, −3.7, −3.4
40–145 km	45–260 km	30–260 km	55–320 km	25–800 km	30–200 km

[a]The studied regions are defined in Figure 2.

We note that the close agreement between the model and altimetry SSH spectra over the shown wavenumber range is a novelty above what was published before. Since the early comparison by *Stammer and Böning* [1992], respective comparisons often revealed too dissipative models leading to too steep slopes in respective model wavenumber spectra toward the high-wavenumber end. This systematic deficiency of the model is absent in our study in which the ATL-4 km agree surprisingly well with the altimetry, specifically in high-energy regions (Figures 9a, 9b, and 9d). In the wavelength band between 70 km $< \lambda <$ 250 km, altimetry follows approximately a $k^{-3.4}$ spectral relation while ATL appears to be decaying following roughly $k^{-3.8}$.

Spectral slopes in high and low-energetic regions are consistent with those presented by *Xu and Fu* [2012], revealing many regional features. *Xu and Fu* [2012] attributed the latitudinal dependence of the SSH spectral slope in the midlatitudes to the latitudinal variation of the transition wavenumber, while the shallow slope in the tropical Pacific and the tropical Atlantic oceans were explained by the stratified turbulence theory of *Waite and Bartello* [2006]. The spectral slopes from ATL simulations are consistent with slopes of k^{-4} found by *Richman et al.* [2012] over the fixed mesoscale band in the Gulf Stream region (close to predictions of surface quasi geostrophic turbulence). The wavenumber slopes computed here for this high-energy region are also consistent to the slopes found previously in high-energy regions, but for the north Pacific [*Sasaki and Klein,* 2012].

On wavelengths below 100 km, altimeter data appear to have higher power spectral density than the model. As can also be seen in Figure 9 (see also Table 2 for spectral slopes), showing altimetric SSH anomaly wavenumber spectra jointly with model results from all available resolutions for selected 20° × 10° regions, all model wavenumber spectra have steeper slopes than altimetry for wavelengths shorter than 100 km. The proximity to a k^{-1} slope in the wavenumber spectra at $\lambda <$ 100 km (Figure 9) can theoretically be attributed to three different processes [*Xu and Fu,* 2011, and reference therein], including (1) an inverse cascade of small-scale energy, (2) the production of gravity waves by unbalanced flows, and (3) a direct cascade of energy from the large-scales.

4.2. Geostrophic Velocity Spectra

Wavenumber spectra computed from the geostrophic velocity anomalies are shown in Figure 10, as they result from satellite data and the 4 km resolution simulation over 20° × 20° regions. Similar to the SSH wavenumber spectra, also the altimetric and model velocity wavenumber spectra agree very well with each other in shape at long wavelengths. However, the model tends to simulate less energy than what is observed on those scales. This holds especially in mid and low latitudes, but not so much in the subpolar basin.

Theoretically, the energy wavenumber spectrum should display a slope of k^{-3} according to quasi-geostrophic turbulence, and a slope of $k^{-5/3}$ according to surface quasi-geostrophic turbulence, the latter

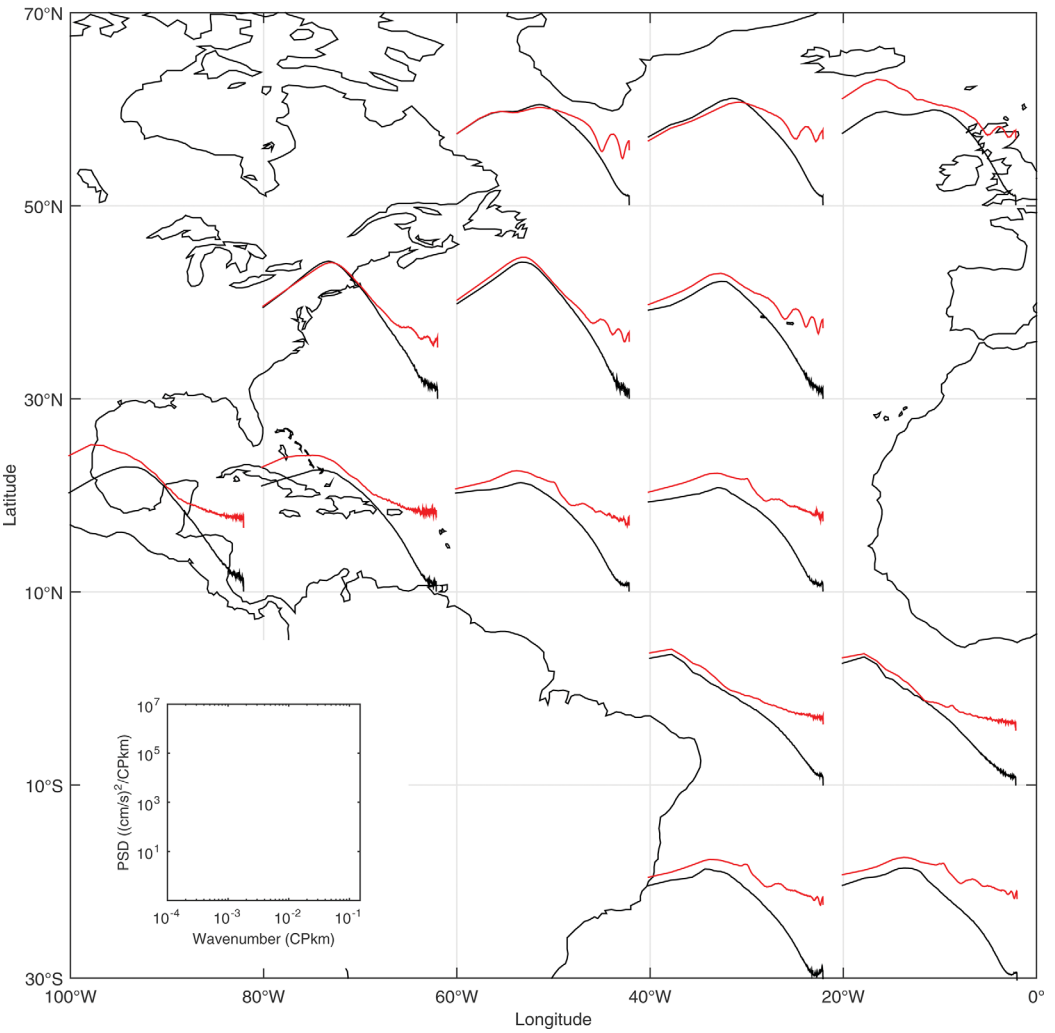

Figure 10. Surface geostrophic velocity wavenumber spectra from $TPJJ_{loess}$ altimetry data (red) and from the ATL simulation with 4 km resolution (black), averaged over 20° × 20° grid boxes.

describing boundary dynamics not included in the quasi-geostrophic theory [*Arbic et al.*, 2012; *Vallis*, 2006]. Previous results suggest that over much of the Atlantic basin, altimetry results are closer to the finite-depth surface quasi-geostrophic turbulence theory [*Tulloch and Smith,* 2006], leading to spectral slopes on the order of $k^{-5/3}$ below 100 km (compare also with *Sasaki and Klein* [2012]). In contrast, our results are consistent with *Wang et al.* [2010] and *Callies and Ferrari* [2013], who show a k^{-3} spectral slope for kinetic energy in the Gulf Stream derived from shipboard measurements. However, their in situ spectral slope estimates are steeper than the respective altimeter estimates, casting doubt on spectral slopes estimated from altimetry at these wavenumbers. In addition, *Callies and Ferrari* [2013] found spectra consistent with interior quasi-geostrophic turbulence at larger scales and consistent with internal-wave dynamics at smaller scales, with the transition occurring at about 20 km. The authors associate k^{-2} spectral slopes in kinetic energy spectra with a variety of unbalanced processes like internal tides. They also suggest that the smaller slopes in altimetry (relative to in situ data) are possibly due to internal tides, which have an important signature in SSH, so that velocities inferred from SSH using the geostrophic balance are not accurate. However, from Figure 11 and Table 2, it appears that, as the resolution of the model simulations increases, there is a tendency for velocity spectral slopes to decrease, therefore pointing to surface quasi-geostrophic turbulence to more adequately describe the dynamics.

More pronounced than for the SSH wavenumber spectra, the agreement between altimetric and model velocity wavenumber spectra is limited to long wavelengths up to a transition scale, right of

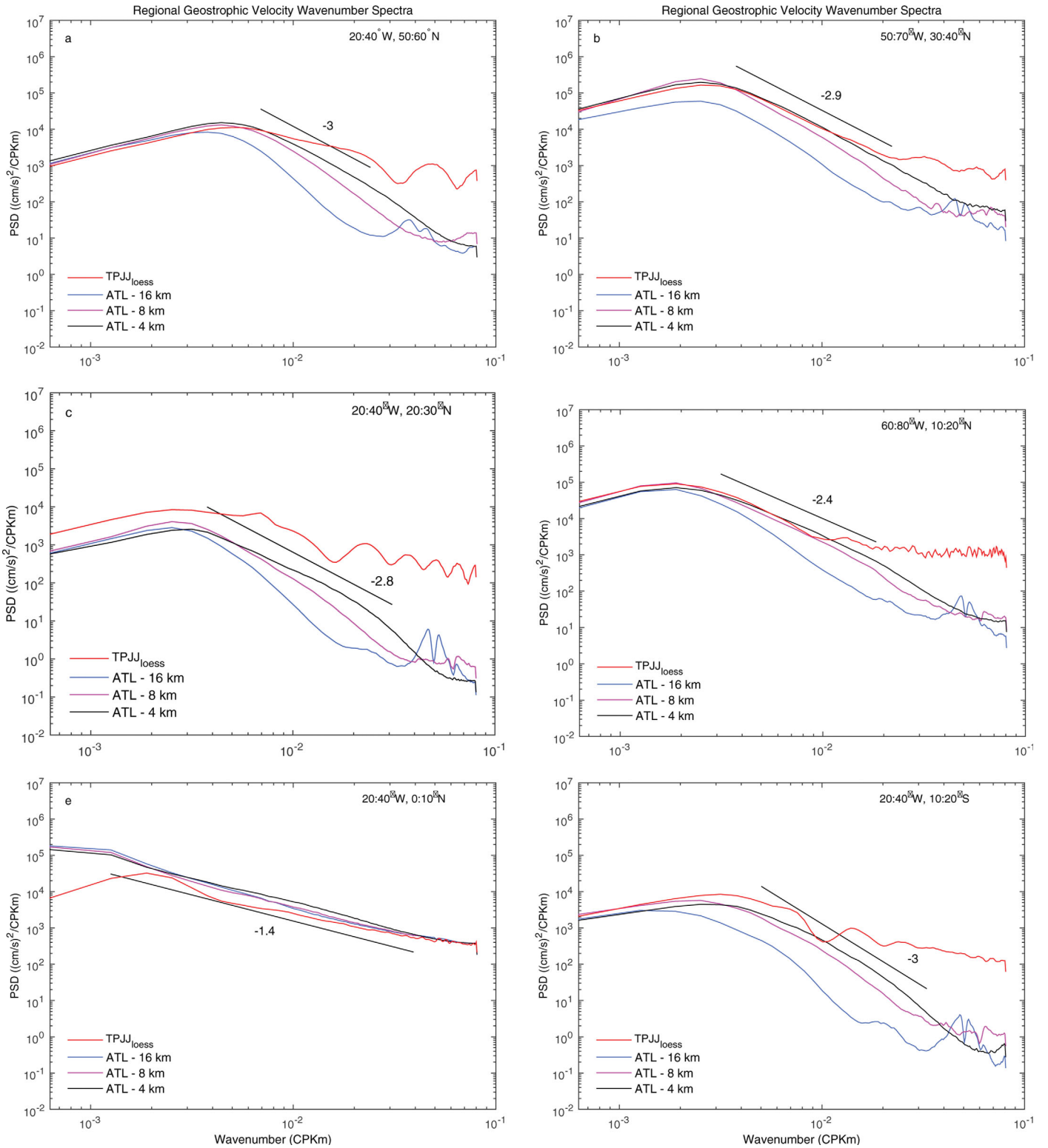

Figure 11. Surface geostrophic velocity wavenumber spectra from $TPJJ_{loess}$ altimetry data (red) and ATL simulations with different resolutions (blue, magenta, and black), averaged in specific dynamically-different regions (see Figure 2 for the region's location). The shown spectral slopes are fitted to the 4 km model.

which both curves diverge. Because SSH and geostrophic velocity spectra result from each other by applying the factor k^2, the altimetric velocity spectrum highlights the noise in the SSH anomalies on wavelengths shorter than the transition scale; therefore results continue to depend on detailed

assumptions about data noise, especially on wavelengths smaller than approximately 100 km [*Le Traon et al.*, 2008; *Xu and Fu*, 2012].

The discrepancy between altimetric and all model velocity wavenumber spectra is further highlighted in Figure 11 (see also Table 2 for spectral slopes) showing altimetric velocity wavenumber spectra together with similar results from all model simulations for various dynamically different 20° × 10° regions. The figure reveals again the impact of enhanced model resolution on the shape of the velocity wavenumber spectra. As can be seen, enhanced model resolution enables enhanced energy on all wavelengths exceeding a primary eddy scale (the mesoscale). In high latitudes, the enhanced resolution also leads to a shift of that primary eddy scale toward smaller wavelengths.

Richman et al. [2012] showed rapidly decaying model spectra with increasing wavenumber compared to flat altimeter spectra at high wavenumbers. They attribute the "flatness" to noise, however, in high-eddy kinetic energy regions, the energy in the mesoscale band is much greater than the noise floor and the spectral slope lies between the prediction of quasi-geostrophic and surface quasi-geostrophic turbulence theories. The authors concluded that the model and altimeter spectral slope estimates may have both dynamical causes as well as instrumental causes.

5. Discussion and Concluding Remarks

This study is concerned with an analysis of sea surface height and surface geostrophic velocity frequency and wavenumber spectra for the Atlantic Ocean using the existing 23 year long TOPEX/Poseidon and Jason-1/2 altimeter data record and a comparison of the results with those obtained from daily averaged model output from a hierarchy of ocean simulations with nominal spatial resolutions ranging from 16 to 4 km.

In general terms, we found fairly flat SSH frequency spectra on long periods (about f^{-1} decay), followed by a regime with steeper slopes toward higher frequencies with close to a f^{-2} spectral decay. The transition between both regimes resides roughly at periods of 75 days; however, this transition can vary with latitude. On periods smaller than 5 days, enhanced SSH variability is present in some regions, notably the tropical band and the subpolar Atlantic. For geostrophic velocity spectra, a somewhat similar picture emerges, albeit with flatter spectral relations, leading to a quasi-white spectrum on periods longer than about 75 days and to a f^{-1} decay on shorter periods. Similar to the SSH frequency spectra, also the geostrophic velocity frequency spectra show enhanced variability on periods below 5 days in the tropical band and in the subpolar ocean. These findings are summarized in Figures 12a and 12c based on the 4 km model results. The figure shows zonally averaged SSH and geostrophic velocity frequency spectra representing latitudinal stripes of 10° in meridional extent. The figure also highlights that the annual cycle is present in SSH spectra from all latitudes, while higher harmonics are conspicuous especially in the tropical band. In contrast, the seasonal cycle and higher harmonics are obvious in velocity frequency spectra only in the tropical band, reflecting the seasonal changes of the flow field there.

From the model-observational data intercomparison, we were able to show that altimetric results are in very good agreement with the 4 km model simulation, especially in the long-period band of the spectra. In agreement with findings from *Arbic et al.* [2012], it is evident from our intercomparison, that, as the resolution increases, the model spectra become more similar to those from altimetry. Nevertheless, discrepancies remain at high frequencies, where regardless of latitude altimetry shows an excess of energy above all model simulations. The cause for this excess of energy in altimetric data remains unclear, however. Several contributions would be plausible, including measurement uncertainties arising from simple (electronic) data noise, from effects of surface waves [*Dibarboure et al.*, 2014] or from surface expressions of internal waves or ageostrophic flow components, as suggested by previous studies [e.g., *Richman et al.*, 2012; *Callies and Ferrari*, 2013; *Wortham and Wunsch*, 2014]. Other causes include uncertainties in all applied corrections. However, we show here that the effect of variability not resolved by the roughly 10 day sampling of the altimeter data should not be underestimated and does contribute significantly to an overestimate of ocean temporal variability on periods below 100 days in the altimeter estimates, especially in the tropics and in the subpolar regions. The aliasing is especially severe in velocity estimates.

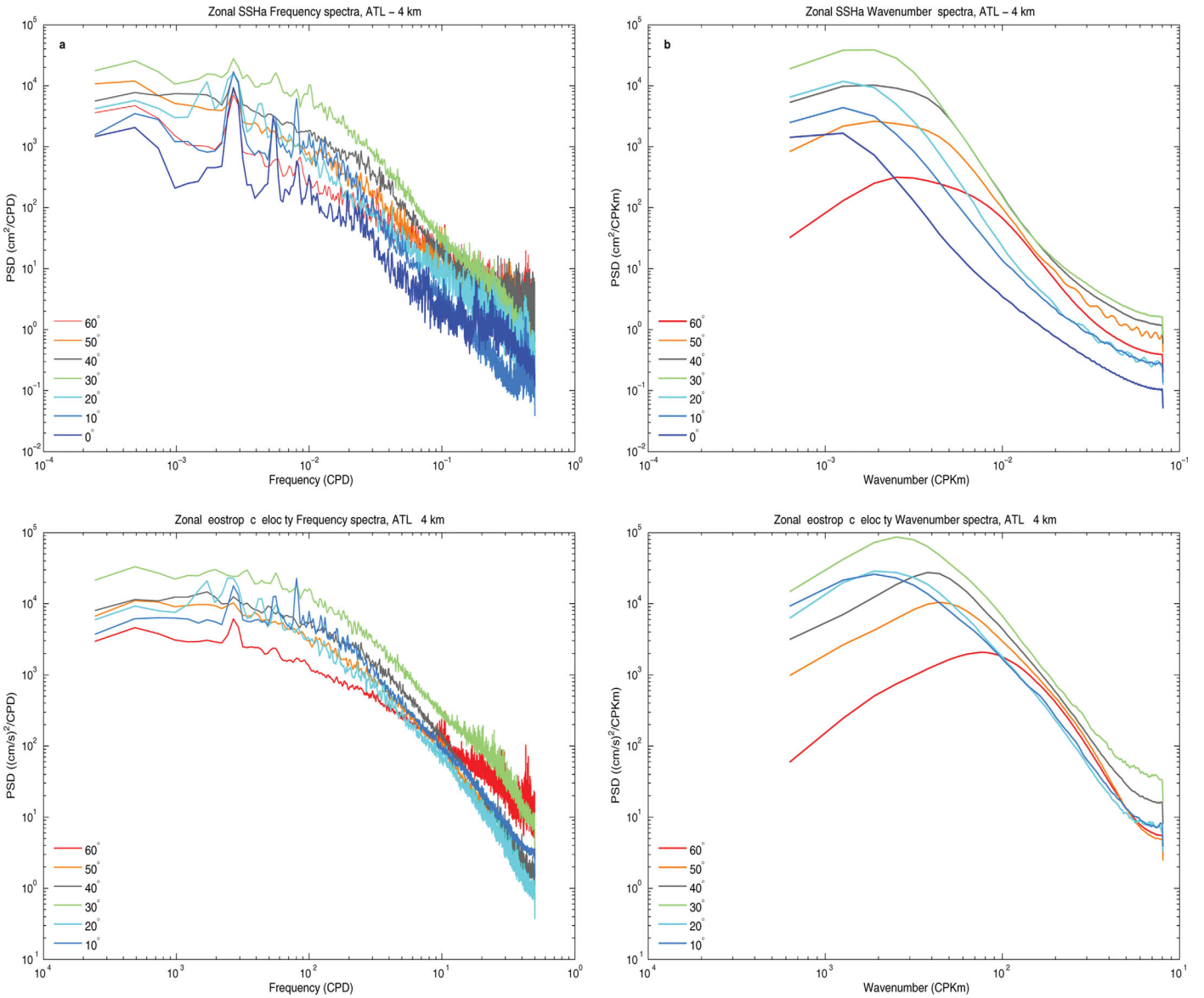

Figure 12. Zonal average of (a, c) frequency and (b, d) wavenumber spectra for (a, b) sea surface height and (c, d) surface geostrophic velocity from the ATL simulation with 4 km resolution.

A very good agreement between altimetric and model spectra exists also in terms of SSH wavenumber spectra, especially on long wavelengths. This holds also for velocity spectra on wavelengths above a meridionally varying transition wavelength. We also note that the model SSH wavenumber spectra essentially follow the altimetric form, even at high wavenumbers, where altimetry shows again an excess of energy. Using the 4 km model results, Figures 12b and 12d hypothesize how observed SSH and velocity wavenumber spectra might look like in the absence of data noise. Similar to the left column of the figure, we show mean spectra averaged zonally and over 10° stripes in latitude north of the equator. The magnitude of energy increases for lower wavenumbers as we travel from the equator to 30°N and then gradually decreases poleward. Below the maximum kinetic energy wavelength, all model velocity wavenumber spectra seem to decay according to a k^{-3} power law.

We conclude from our analysis that the model simulations capture more of the ocean dynamics as the resolution increases, shifting energy gradually to higher wavenumbers and larger amplitudes. Past idealized model integrations [*Capet et al.*, 2008; *Klein et al.*, 2008] have already suggested the importance of horizontal resolution to resolve submesoscale processes and achieve large energy levels at high wavenumbers, a

claim which is here reinforced. Nevertheless, the models still fail to capture the dynamics of the submesoscale in many subdomains, especially in low-energy regimes. On the other hand, especially altimetric velocity wavenumber spectra are impacted by data noise roughly on wavelengths below 50 km. Substantial work, therefore, has to continue in order to understand the realism of model results on the wavelengths down to the submesoscale, as resolution further increases. At the same time, substantial work has to be spent in understanding and removing data noise in the altimeter measurements on those small spatial scales.

Acknowledgments
The data used are available from the RADS data server http://rads.tudelft.nl/rads/rads.shtm. This work was supported in parts through the ESA CCI Sea Level initiative and by the DFG funded Excellence Initiative Project CliSAP of the University of Hamburg. All model integrations were performed at the German Climate Computing Center (DKRZ) in Hamburg, Germany, in the frame of the BMBF funded projects "Nordatlantik" and "RACE" and of DKRZ project 704.

References

Arbic, B. K., R. Scott, G. Flierl, A. Morten, J. Richman, and J. Shriver (2012), Nonlinear cascades of surface oceanic geostrophic kinetic energy in the frequency domain, *J. Phys. Oceanogr.*, *42*, 1577–1600, doi:10.1175/JPO-D-11-0151.1.

Arbic, B. K., M. Müller, J. G. Richman, J. F. Shriver, A. J. Morten, R. B. Scott, G. Sérazin, and T. Penduff (2014), Geostrophic turbulence in the frequency-wavenumber domain: Eddy-driven low-frequency variability, *J. Phys. Oceanogr.*, *44*, 2050–2069, doi:10.1175/JPO-D-13-054.1.

Blumen, W. (1978), Uniform potential vorticity flow: Part I: Theory of wave interactions and two-dimensional turbulence, *J. Atmos. Sci.*, *35*, 774–783.

Boyer, T., S. Levitus, H. Garcia, R. Locarnini, C. Stephens, and J. Antonov (2005), Objective analyses of annual, seasonal, and monthly temperature and salinity for the world ocean on a 0.25° grid, *Int. J. Climatol.*, *25*(7), 931–945.

Callies, J., and R. Ferrari (2013), Interpreting energy and tracer spectra of upper-ocean turbulence in the submesoscale range (1-200km), *J. Phys. Oceanogr.*, *43*, 2456–2474, doi:10.1175/JPO-D-13-063.1.

Cane, M. A., and D. W. Moore (1981), A note on low-frequency equatorial basin modes, *J. Phys. Oceanogr.*, *11*, 1578–1584.

Capet, X., J. C. McWilliams, M. J. Molemaker, and A. F. Shchepetkin (2008), Mesoscale to submesoscale transition in the California current system. Part I: Flow structure, eddy flux, and observational tests, *J. Phys. Oceanogr.*, *38*, 29–43.

Dee, D. P., et al. (2011), The ERA-Interim reanalysis: Configuration and performance of the data assimilation system, *Q. J. R. Meteorol. Soc.*, *137*(656), 553–597, doi:10.1002/qj.828.

Dibarboure, G., F. Boy, J. D. Desjonqueres, S. Labroue, Y. Lasne, N. Picot, J. C. Poisson, and P. Thibaut (2014), Investigating short-wavelength correlated errors on low-resolution mode altimetry, *J. Atmos. Oceanic Technol.*, *31*, 1337–1362, doi:10.1175/JTECH-D-13-00081.1.

Ferrari, R. and C. Wunsch (2009), Ocean circulation kinetic energy: Reservoirs, sources, and sinks, *Annu. Rev. Fluid Mech.*, *41*, 253–282, doi: 10.1146/annurev.fluid.40.111406.102139.

Jin, F. F. (2001), Low-frequency modes of tropical ocean dynamics, *J. Clim.*, *14*, 3874–3881.

Kalnay, E., et al. (1996). The ncep/ncar 40-year reanalysis project, *Bull. Am. Meteorol. Soc.*, *77*, 437–470.

Klein, P., B. L. Hua, G. Lapeyre, X. Capet, S. Le Gentil, and H. Sasaki (2008), Upper ocean turbulence from high-resolution 3D simulations, *J. Phys. Oceanogr.*, *38*(8), 1748–1763.

Köhl, A., and N. Serra (2014), Causes of decadal changes of the freshwater content in the [A]rctic ocean, *J. Clim.*, *27*, 3461–3475.

Koldunov, N. V., N. Serra, A. Köhl, and D. Stammer (2014), Multimodel simulations of Arctic Ocean sea surface height variability in the period 1970-2009, *J. Geophys. Res. Oceans*, *119*, 8936–8954, doi:10.1002/2014JC010170.

Le Traon, P. Y., and M. C. Rouqueti (1990), Spatial scales of mesoscale variability in the North Atlantic as deduced from geosat data, *J. Geophys. Res.*, *95*(C11), 20,267–20,285.

Le Traon, P. Y., P. Klein, B. L. Hua, and G. Dibarboure (2008), Do altimeter wavenumber spectra agree with the interior or surface quasi-geostrophic theory?, *J. Phys. Oceanogr.*, *38*, 1137–1142, doi:10.1175/2007JPO3806.1.

Marshall, J., A. Adcroft, C. Hill, L. Perelman, and C. Heisey (1997), A finite-volume, incompressible Navier-Stokes model for studies of the ocean on parallel computers, *J. Geophys. Res.*, *102*(C3), 5753–5766.

Müller, P., and C. Frankignoul, C. (1981), Direct atmospheric forcing of geostrophic eddies. *J. Phys. Oceanogr.*, *11*(3), 287–308.

Ponte, R. M., and F. Lyard (2002), Effects of unresolved high-frequency signals in altimeter records inferred from tide gauge data, *J. Atmos. Oceanic Technol.*, *19*, 534–539.

Provost, C., and P.-Y. Le Traon (1993), Spatial and temporal scales in altimetric variability in the [B]razil-[M]alvinas current confluence region: Dominance of the semiannual period and large spatial scales, *J. Geophys. Res.*, *98*(C10), 18,037–18,051.

Ray, R. D. (1998), Spectral analysis of highly aliased sea-level signals, *J. Geophys. Res.*, *103*(C11), 24,991–25,003.

Richman, J. G., B. K. Arbic, J. F. Shriver, R. J. Metzger, and A. J. Wallcraft (2012), Inferring dynamics from wavenumber spectra of an eddying global ocean model with embedded tides, *J. Geophys. Res.*, *117*, C12012, doi:10.1029/2012JC008364.

Sasaki, H., and P. Klein (2012), SSH wavenumber spectra in the north pacific from a high-resolution realistic simulation. *J. Phys. Oceanogr.*, *42*, 1233–1241, doi:10.1175/JPO-D-11-0180.1.

Scharffenberg, M., and D. Stammer (2010), Seasonal variations of the large-scale geostrophic flow field and eddy kinetic energy inferred from the TOPEX/Poseidon and Jason-1 tandem mission data, *J. Geophys. Res.*, *115*, C02008, doi:10.1029/2008JC005242.

Scharffenberg, M., and D. Stammer (2011), Statistical parameters of the geostrophic ocean flow field, estimated by Jason-1-TOPEX/Poseidon tandem mission, *J. Geophys. Res.*, *116*, C12011, doi:10.1029/2011JC007376.

Scharroo, R., E. W. Leuliette, J. L. Lillibridge, D. Byrne, M. C. Naeije, and G. T. Mitchum (2013) RADS: Consistent multi-mission products. *in Proceedings of the Symposium on 20 Years of Progress in Radar Altimetry, Venice, 20-28 Sept. 2012, Eur. Space Agency Spec. Publ., ESA SP-710*, edited by L. Ouwehand, 4 pp.

Sena Martins, M., N. Serra, and D. Stammer (2015), Spatial and temporal scales of sea surface salinity variability in the Atlantic Ocean, *J. Geophys. Res. Oceans*, *120*, 4306–4323, doi:10.1002/2014JC010649.

Serra, N., R. H. Käse, A. Köhl, and D. Stammer (2010), On the low-frequency phase relation between the Denmark strait and the faroe-bank channel overflows, *Tellus Ser. A*, *62*, 530–550.

Stammer, D. (1997), Global characteristics of ocean variability estimated from regional TOPEX/Poseidon altimeter measurements, *J. Phys. Oceanogr.*, *27*, 1743–1769.

Stammer, D., and C. W. Böning (1992), Mesoscale variability in the [A]tlantic ocean from geosat altimetry and [W]oce high-resolution numerical modeling, *J. Phys. Oceanogr.*, *22*, 732–752.

Tulloch, R., and K. S. Smith (2006), A theory for the atmospheric energy spectrum: Depth-limited temperature anomalies at the tropopause, *Proc. Natl. Acad. Sci. U. S. A.*, *103*, 14,690–14,694.

Vallis, G. K. (2006), *Atmospheric and Oceanic Fluid Dynamics*, 745 pp., Cambridge Univ. Press, Cambridge, U. K.

Waite, M. L., and P. Bartello (2006), The transition from geostrophic to stratified turbulence. *J. Fluid Mech.*, *568*, 89–108, doi:10.1017/S0022112006002060.

Wang, D. P., C. N. Flagg, K. Donohue, and H. T. Rossby (2010), Wavenumber spectrum in the Gulf Stream from shipboard ADCP observations and comparison with altimetry measurements, *J. Phys. Oceanogr.*, *40*(4), 840–844.

Wortham, C., and C. Wunsch (2014), A multidimensional spectral description of ocean variability, *J. Phys. Oceanogr.*, *44*, 944–966, doi:10.1175/JPO-D-13-0113.1.

Wunsch, C. (1981), Low-frequency variability in the sea, in *Evolution of Physical Oceanography*, edited by B. A. Warren, and C. Wunsch, 549 pp., MIT Press, Cambridge, Mass.

Xu, Y., and L. Fu (2012), The effects of altimeter instrument noise on the estimation of the wavenumber spectrum of sea surface height, *J. Phys. Oceanogr.*, *42*, 2229–2233, doi:10.1175/JPO-D-12-0106.1.

Xu, Y., and L.-L. Fu (2011), Global variability of the wavenumber spectrum of oceanic mesoscale turbulence, *J. Phys. Oceanogr.*, *41*, 802–809, doi:10.1175/2010JPO4558.1.

Zhou, X.-H., D.-P. Wang, and D. Chen (2015), Global wavenumber spectrum with corrections for altimeter high-frequency noise, *J. Phys. Oceanogr.*, *45*, 495–503, doi:10.1175/JPO-D-14-0144.1.